





## Anisotropic anomalous transport in the kagome-based topological antiferromagnetic $\text{Mn}_3\text{Ga}$ epitaxial thin films

M. Raju <sup>1,\*</sup> Ralph Romero, III <sup>1</sup> Daisuke Nishio-Hamane,<sup>2</sup> Ryota Uesugi <sup>2</sup> Mihiro Asakura,<sup>3</sup> Zhenisbek Tagay,<sup>1</sup> Tomoya Higo,<sup>2,3</sup> N. P. Armitage,<sup>1,5</sup> Collin Broholm,<sup>1</sup> and Satoru Nakatsuji <sup>1,2,3,4,5,†</sup>

<sup>1</sup>*Institute for Quantum Matter, Department of Physics and Astronomy, Johns Hopkins University, Baltimore, Maryland 21218, USA*

<sup>2</sup>*Institute for Solid State Physics, University of Tokyo, Kashiwa, Chiba 277-8581, Japan*

<sup>3</sup>*Department of Physics, University of Tokyo, Bunkyo-ku, Tokyo 113-0033, Japan*

<sup>4</sup>*Trans-Scale Quantum Science Institute, University of Tokyo, Bunkyo-ku, Tokyo 113-0033, Japan*

<sup>5</sup>*Canadian Institute for Advanced Research, Toronto, Ontario M5G 1M1, Canada*



(Received 26 August 2023; accepted 2 January 2024; published 26 January 2024)

$\text{Mn}_3X$  ( $X = \text{Sn}, \text{Ge}, \text{Ga}$ ) kagome Weyl semimetals have attracted significant research interest due to their large anomalous Hall, thermal, and optical effects originating from their nontrivial band topology. These large topological effects together with the antichiral antiferromagnetic order that can be manipulated through various experimental means provide unique platforms for developing high-speed spintronics.  $\text{Mn}_3\text{Ga}$  is known to have the largest Néel temperature ( $T_N \approx 480$  K), which is useful for developing antiferromagnetic spintronics. Here, we establish the epitaxial growth of antiferromagnetic  $\text{Mn}_3\text{Ga}$  films by magnetron sputtering and present their structure, magnetotransport, terahertz properties, and exchange bias effect in  $\text{Mn}_3\text{Ga}/\text{NiFe}$  bilayers, establishing their remarkable properties essential for future investigations towards device applications.

DOI: [10.1103/PhysRevMaterials.8.014204](https://doi.org/10.1103/PhysRevMaterials.8.014204)

### I. INTRODUCTION

Weyl semimetal  $\text{Mn}_3X$  ( $X = \text{Sn}, \text{Ge}, \text{Ga}$ ) compounds hosting antichiral spin structure on their kagome lattices have attracted research interest for their fascinating properties useful for developing antiferromagnetic (AFM) topological spintronics [1–4]. These materials show large nontrivial effects such as anomalous Hall effect (AHE) [5] up into the terahertz frequency range [6], spin Hall and magnetic spin Hall effects [7], anomalous Nernst effect [8,9], and magneto-optical effects [6,10–12]. These electromagnetic responses originate from a sizable momentum space Berry curvature, linked to the chiral AFM spin texture formed by the Mn spin moments on the Mn kagome lattice in real space. This coupling of real space spin structure to the momentum space band topology provides a necessary handle to harness the technological prospects of these materials [3,13,14]. Hexagonal  $\text{Mn}_3X$  materials show anisotropic magnetotransport responses along different crystal orientations as well as kagome spin structure formed by the Mn moments [13,15–17]; hence, control over crystal orientation in thin film structures is essential to fully exploit the Berry phase effects for device applications. For example, it is desirable to have the kagome spin structure aligned normal to the film plane, that is  $ab$ -axis orientation, for spintronics devices based on AHE [18,19], and kagome spin structure within the film plane, which is  $c$ -axis orientation, for devices based on spin Hall or thermoelectric effects [7,20]. Recent experimental successes in the electrical and optical detection/manipulation of antiferromagnetic order

using  $\text{Mn}_3\text{Sn}$  thin films are promising towards developing antiferromagnetic random access memory [18,19,21–24]. In addition, recent observations on superconducting proximity effects in the  $\text{Mn}_3\text{Ge}/\text{Nb}$  interfacial system open new possibilities of topological superconducting spintronics [25].

Within the family of the hexagonal  $D0_{19}$   $\text{Mn}_3X$  ( $X = \text{Sn}, \text{Ge}, \text{Ga}$ ) compounds, so far  $\text{Mn}_3\text{Ga}$  has attracted limited attention compared to  $\text{Mn}_3\text{Sn}$  and  $\text{Mn}_3\text{Ge}$ , probably due to a smaller anomalous Hall conductivity (AHC) reported for this material [15,26,27] and growth challenges due to competing Mn-Ga structural and magnetic phases [27]. The hexagonal  $\text{Mn}_3\text{Ga}$  is expected to be an antiferromagnetic Weyl semimetal with a larger spin Hall response [15] and is known to have a larger magnetic ordering temperature ( $T_N \approx 480$  K) compared to  $T_N \approx 420$  and 360 K of  $\text{Mn}_3X$  ( $X = \text{Sn}, \text{Ge}$ ), respectively.

For memory applications, which are the ultimate and realistic goal of electrical switching, higher magnetic transition temperatures are required in terms of thermal stability. In light of this, developing a similar class of thin film materials with the largest possible  $T_N$ , like antiferromagnetic  $\text{Mn}_3\text{Ga}$ , is an essential requirement. In this paper, we develop the hexagonal  $\text{Mn}_3\text{Ga}$  AFM thin films by using the magnetron sputtering technique. We use  $\text{MgO}(110)$  substrates with  $\text{W}(7$  nm) buffer layer for achieving  $ab$ -axis oriented  $\text{Mn}_3\text{Ga}$  and  $\text{Al}_2\text{O}_3(0001)$  substrates with  $\text{Ru}(5$  nm) buffer layer for  $c$ -axis oriented  $\text{Mn}_3\text{Ga}$  films. Films are characterized through x-ray diffraction (XRD), cross-sectional high-resolution transmission electron microscopy (HRTEM), magnetization measurements, AHE, magnetoresistance (MR) effect, and terahertz Faraday effect. Our investigations reveal that both  $ab$ -axis and  $c$ -axis films grow epitaxially, albeit the

\*mraju5@jhu.edu

†snakats1@jhu.edu

*ab*-axis  $\text{Mn}_3\text{Ga}$  films show minor peaks corresponding to  $(31\bar{4}0)$  oriented crystallites. Films have in-plane strain up to 0.7 and 1.6% depending on the substrate and the buffer layer. The *ab*-axis orientated  $\text{Mn}_3\text{Ga}$  shows large spontaneous AHE, which vanishes for the *c*-axis case, confirming the expected anisotropy in AHE for these two crystal orientations [15]. The AHE magnitude for the *ab*-axis case shows a nonmonotonic behavior with temperature, with an estimated AHC of  $17 (\Omega \text{ cm})^{-1}$  at 300 K,  $28 (\Omega \text{ cm})^{-1}$  between 100 and 200 K, and  $19 (\Omega \text{ cm})^{-1}$  at 10 K. The terahertz time-domain spectroscopy investigations between 10 and 225 K reveal a large Faraday effect, consistent with the AHE trends seen in the DC transport measurements and terahertz optical properties comparable to previously reported  $\text{Mn}_3\text{Sn}$  films [28]. The MR measurements show an increase in negative magnetoresistance (NMR) for the applied field ( $B$ ) parallel to current ( $I$ ),  $B \parallel I$ , compared to  $B \perp I$  configuration, suggestive of chiral anomaly behavior expected for this class of materials. Finally, we demonstrate the exchange bias (EB) effect in  $\text{Mn}_3\text{Ga}(40 \text{ nm})/\text{NiFe}(10 \text{ nm})$  establishing the antiferromagnetic character of our hexagonal  $\text{Mn}_3\text{Ga}$  films; these results provide insights into the effect of  $\text{Mn}_3\text{Ga}(40 \text{ nm})$  crystal orientation on exchange bias properties.

## II. RESULTS AND DISCUSSION

### A. Structural characterization

Figures 1(a) and 1(g) show the schematics of the sample structure  $\text{MgO}(110)/\text{W}(7 \text{ nm})/\text{Mn}_3\text{Ga}(40 \text{ nm})/\text{AlO-cap}$ ,  $\text{Al}_2\text{O}_3(0001)/\text{Ru}(5 \text{ nm})/\text{Mn}_3\text{Ga}(40 \text{ nm})/\text{AlO-cap}$  used in this paper for *ab*-axis and *c*-axis oriented  $\text{Mn}_3\text{Ga}$ , respectively, and the expected antichiral spin structure formed by Mn moments along the out-of-plane direction. Figures 1(b), 1(c), 1(h), and 1(i) show the results obtained by the x-ray diffraction investigations. A combination of out-of-plane and in-plane diffraction peaks captured in Figs. 1(b), 1(c), 1(h), and 1(i) confirms the epitaxial growth of the films with *ab*-axis orientation on  $\text{MgO}/\text{W}$  and *c*-axis orientation on  $\text{Al}_2\text{O}_3/\text{Ru}$ . Rocking curve measurements are carried out on each diffraction peak to assess their width (see Fig. S1, Supplemental Material [29]). All the diffraction peaks can be identified uniquely with the hexagonal  $\text{Mn}_3\text{Ga}$  phase, indicating a single phase without any impurity phases.

In the case of the *ab*-axis oriented film, along with  $(02\bar{2}0)$  ( $2\theta = 38.612^\circ$ ) and  $(04\bar{4}0)$  ( $2\theta = 82.656^\circ$ ) diffraction peaks we also see a minor peak corresponding to  $(31\bar{4}1)$  ( $2\theta = 77.478^\circ$ ), suggesting the presence of undesired crystallites. On the other hand, our *c*-axis films show only  $(0002)$  ( $2\theta = 41.464^\circ$ ) and  $(0004)$  ( $2\theta = 90.035^\circ$ ) diffraction peaks. Width of the diffraction peaks (see Fig. S1, Supplemental Material [29]) suggests *c*-axis oriented films [full width at half maximum (FWHM) =  $0.006^\circ$ ] have superior quality compared to *ab*-axis films (FWHM =  $1.3^\circ$ ), these structural differences are influenced by the underlying buffer layers, larger width of  $\text{Mn}_3\text{Ga}(02\bar{2}0)$  diffraction peaks correlates with the larger width of the  $\text{W}(7 \text{ nm})$  (FWHM =  $1.9^\circ$ ) layer diffraction peaks, and sharper diffraction peaks for *c*-axis  $\text{Mn}_3\text{Ga}(0002)$  correlate well with the sharper diffraction peaks of the  $\text{Ru}(5 \text{ nm})$  (FWHM =  $0.005^\circ$ ) layer.

Based on  $(02\bar{2}0)$  and  $(20\bar{2}1)$  diffraction peaks of *ab*-axis oriented samples shown in Figs. 1(b) and 1(c), our estimated lattice parameters indicate  $a = 5.384 \text{ \AA}$ , and  $c = 4.380 \text{ \AA}$ . In case of the *c*-axis oriented sample shown in Figs. 1(h) and 1(i), diffraction peaks  $(0002)$  and  $(20\bar{2}3)$  lead to estimated lattice parameters of  $a = 5.306 \text{ \AA}$  and  $c = 4.355 \text{ \AA}$ . Comparison of the estimated values with lattice parameters of a bulk hexagonal  $\text{Mn}_3\text{Ga}$  compound  $a^{\text{bulk}} = 5.391 \text{ \AA}$  and  $c^{\text{bulk}} = 4.348 \text{ \AA}$  [30] shows that our  $\text{Mn}_3\text{Ga}$  films on  $\text{MgO}(110)/\text{W}(7 \text{ nm})$  show an estimated in-plane tensile strain  $(\frac{|c^{\text{film}} - c^{\text{bulk}}|}{c^{\text{bulk}}}) \times 100$  of  $\approx 0.7\%$  and an out-of-plane compressive strain  $(\frac{|a^{\text{film}} - a^{\text{bulk}}|}{a^{\text{bulk}}}) \times 100$  of  $\approx 0.1\%$ . On the other hand,  $\text{Mn}_3\text{Ga}$  films on  $\text{Al}_2\text{O}_3(0001)/\text{Ru}(5 \text{ nm})$  show an in-plane compressive strain  $(\frac{|a^{\text{film}} - a^{\text{bulk}}|}{a^{\text{bulk}}}) \times 100$  of  $\approx 1.6\%$  and an out-of-plane tensile strain  $(\frac{|c^{\text{film}} - c^{\text{bulk}}|}{c^{\text{bulk}}}) \times 100$  of  $\approx 0.1\%$ . These observations suggest that underlying buffer layers play a key role in in-plane lattice strain in the subsequently grown  $\text{Mn}_3\text{Ga}$  films. Studies have shown that the strain in these thin film structures plays an important role in controlling the effective magnetic anisotropy and electrical control of magnetic moments [19,31,32].

Development of *ab*-axis oriented  $\text{Mn}_3\text{X}$  epitaxial films had been a challenge, almost all the works so far were focused on  $\text{Mn}_3\text{Sn}$ , often requiring high-temperature treatment for epitaxial growth, and a buffer layer with appropriate lattice matching is essential to promote hexagonal structure. One needs to find an optimum temperature to promote crystal growth without causing the intermixing of elements at the interface with the buffer layer [19,33]. A small volume fraction of unwanted crystal orientations is expected for the annealing temperatures used in this paper [19]. The presence of crystal grains with different orientations may produce interesting magnetotransport in these materials. For example, the volume fraction of the grains with a kagome plane normal to the film surface contributes largely to the anomalous Hall signal, while grains with a kagome plane within the film produce spin Hall effect, which may lead to self-switching spin-polarized current [22].

Figures 1(d)–1(f) and 1(j)–1(l) show the results of the HRTEM investigations for the films on the  $\text{MgO}$  and  $\text{Al}_2\text{O}_3$  substrates, respectively. As shown in Fig. 1(e), electron diffraction of  $\text{MgO}$ ,  $\text{W}$ , and  $\text{Mn}_3\text{Ga}$  and their simulated patterns [34] show epitaxial growth with the crystal orientation of  $\text{MgO}(110)[00\bar{1}]||\text{W}(211)[01\bar{1}]||\text{Mn}_3\text{Ga}(01\bar{1}0)[000\bar{1}]$ . Similarly, in Fig. 1(k), the electron diffraction patterns of the film on the  $\text{Al}_2\text{O}_3$  substrates show crystal orientation  $\text{Al}_2\text{O}_3(0001)[00\bar{1}]||\text{Ru}(0001)[0\bar{1}1]||\text{Mn}_3\text{Ga}(0001)[1\bar{1}20]$ . These electron diffraction results and the cross-section images shown in Figs. 1(f) and 1(l) are consistent with the XRD investigations. The electron diffraction patterns of  $\text{Al}_2\text{O}_3$  and  $\text{Ru}$  and  $\text{Mn}_3\text{Ga}$  overlap [Fig. 1(k)]; although it is difficult to distinguish the patterns for each layer, we expect the film to be oriented consistent with the XRD results since no extra diffraction spots are seen.

### B. Magnetization

Figure 2 shows the magnetization data for both *ab*-axis oriented  $\text{Mn}_3\text{Ga}$  grown on  $\text{MgO}/\text{W}$  and *c*-axis oriented  $\text{Mn}_3\text{Ga}$  on  $\text{Al}_2\text{O}_3/\text{Ru}$ , recorded in out-of-plane applied field.

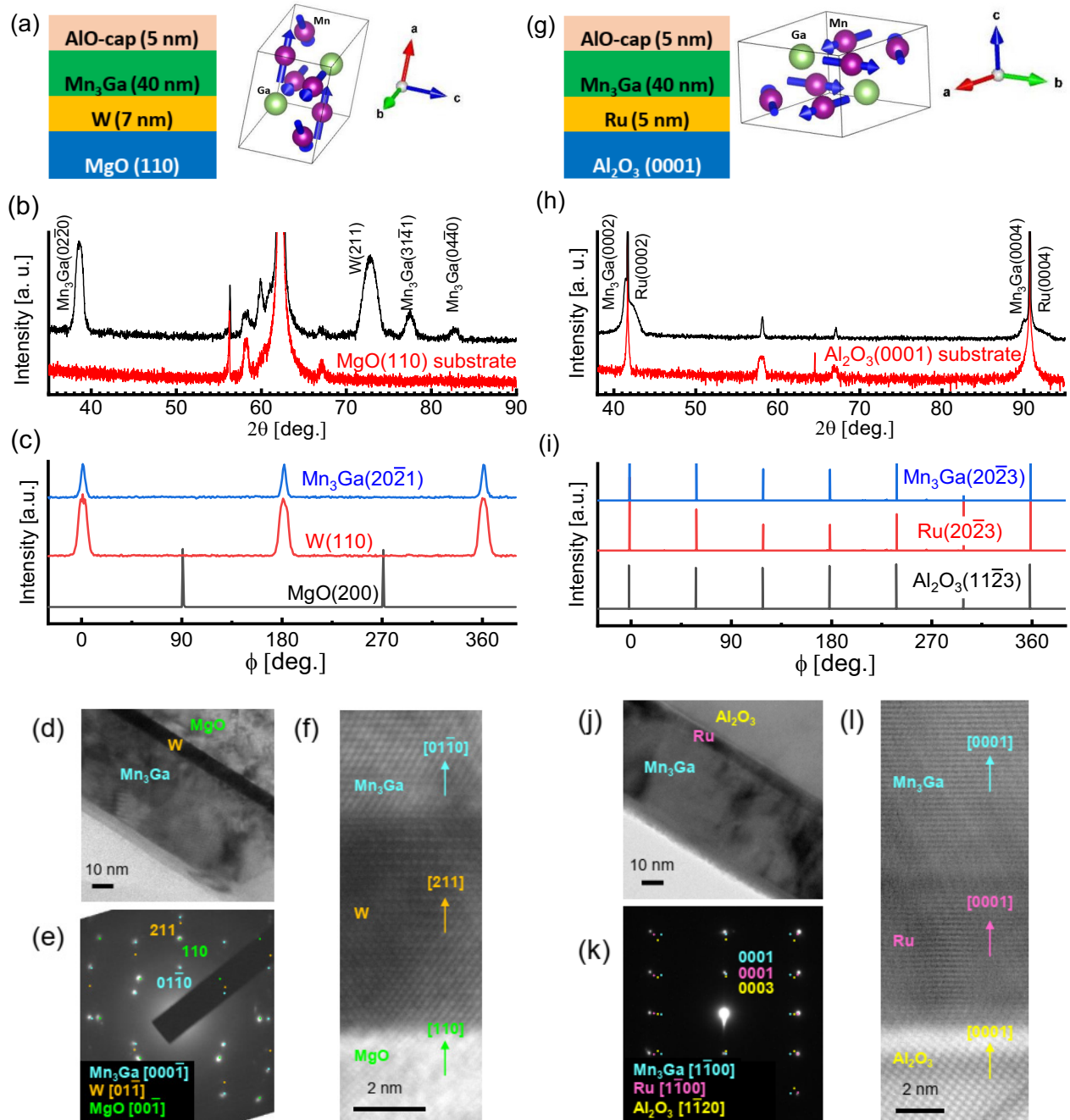


FIG. 1. X-ray diffraction and cross-sectional HRTEM results for the *ab*-axis and *c*-axis oriented  $\text{Mn}_3\text{Ga}$  samples. Schematics for thin film stacks and antichiral spin structures expected (a) for the *ab*-axis oriented  $\text{Mn}_3\text{Ga}$  film stack, i.e.,  $\text{MgO}(110)/\text{W}(7\text{ nm})/\text{Mn}_3\text{Ga}(40\text{ nm})/\text{Al}_2\text{O}_3(5\text{ nm})$ , and (g) for the *c*-axis oriented  $\text{Mn}_3\text{Ga}$  film stack  $\text{Al}_2\text{O}_3(0001)/\text{Ru}(5\text{ nm})/\text{Mn}_3\text{Ga}(40\text{ nm})/\text{Al}_2\text{O}_3(5\text{ nm})$ . (b), (c)  $\theta$ - $2\theta$  and in-plane  $\phi$  scans for the *ab*-axis oriented  $\text{Mn}_3\text{Ga}(40\text{ nm})$  film. [(d)–(f)] Cross-sectional view of the HRTEM sample, experimental and simulated electron diffraction patterns, and cross-sectional high-resolution TEM image for *ab*-axis oriented  $\text{Mn}_3\text{Ga}(40\text{ nm})$  film. (h), (i)  $\theta$ - $2\theta$  and in-plane  $\phi$  scans of the *c*-axis oriented  $\text{Mn}_3\text{Ga}(40\text{ nm})$  film.  $\theta$ - $2\theta$  scans for bare  $\text{MgO}(110)$  and  $\text{Al}_2\text{O}_3(0006)$  substrates shown in panels (b) and (h) are also recorded for reference. [(j)–(l)] Cross-sectional view of the HRTEM sample, experimental and simulated electron diffraction patterns, and cross-sectional high-resolution TEM image for *c*-axis oriented  $\text{Mn}_3\text{Ga}(40\text{ nm})$  film.

Magnetization for the *ab*-axis sample is shown to be relatively larger compared to the *c*-axis sample. As a function of the field, a smooth variation of magnetization with a coercivity of 0.01 T is seen for the *c*-axis case while the *ab*-axis shows a coercivity of 0.1 T [inset to Fig. 2(a)]. These observations

are consistent with the expected anisotropy in magnetization along these crystal orientations. However, an estimated spontaneous magnetic moment suggests a moment up to  $\approx 0.042\ \mu_B/\text{Mn}$  for *ab*-axis-oriented film and  $\approx 0.016\ \mu_B/\text{Mn}$  for *c*-axis oriented film, several times larger compared to



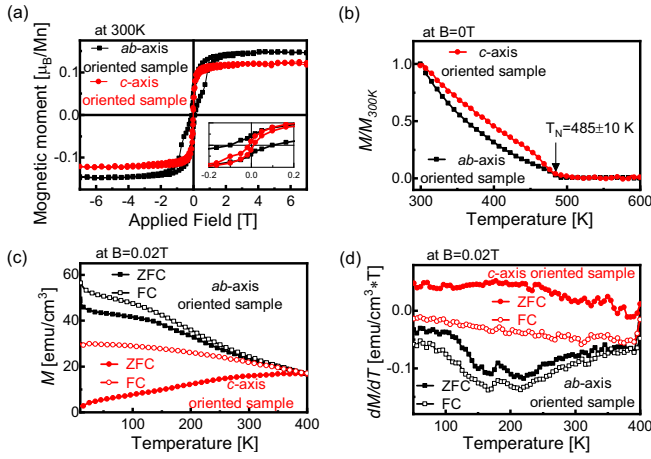


FIG. 2. Magnetization results for the  $ab$ -axis and the  $c$ -axis oriented  $Mn_3Ga$  films. (a) Comparison of the magnetization vs field  $[M(B)]$  curve measured at 300 K for  $ab$ -axis and  $c$ -axis oriented samples. The inset to panel (a) shows the low field evolution of the  $M(B)$  curve. (b) In-plane magnetization vs temperature  $[M(T)]$  measured between 300 and 600 K for  $ab$ -axis and  $c$ -axis oriented samples. Data are normalized to the magnetization value at 300 K, and measurement is performed at  $B = 0$  T after saturating the sample at  $B = 5$  T. The error bar in the estimated value of Néel temperature represents uncertainty in the sample temperature. (c) Temperature dependence of the zero-field cooled (ZFC) and field cooled (FC) magnetization for the  $ab$ -axis and  $c$ -axis oriented  $Mn_3Ga$  samples, measured at  $B = 0.02$  T. (d) Numerical derivative  $dM/dT$  profiles of the  $M$  vs  $T$  data shown in panel (c).

few-milli- $\mu_B/Mn$  expected for their bulk crystal forms [26]. Such an enhancement in magnetization appears to be common in similar noncollinear antiferromagnetic thin films [35], probably caused by several factors such as chemical, structural disorder, and demagnetization effects in the thin film limit [19,31,32,35]. In fact, increased magnetic moment and anisotropy may also result from the lattice strain in the film leading to piezomagnetic effects [36]. Figure 2(b) shows the temperature-dependent in-plane magnetization measured between 300 and 600 K. Samples were first magnetized by applying an in-plane field of 5 T and then the field was reduced to zero. The measured remnant magnetization with temperature suggests a  $T_N$  of  $\approx 485$  K for both  $ab$ -axis and  $c$ -axis oriented samples grown on different substrates. This measured  $T_N$  further confirms the phase purity of our hexagonal antiferromagnetic  $Mn_3Ga$  films. The  $T$ -dependent magnetization data in Fig. 2(c) show that the  $ab$ -axis samples possess a larger magnetization compared to  $c$ -axis films for the entire temperature range of 10–400 K. Further,  $ab$ -axis oriented films show subtle diplike variation in magnetization around 175 K, followed by a broad shallow peak around 150 K. These variations are highlighted through a numerical derivative of magnetization ( $dM/dT$ ) with  $T$  as shown in Fig. 2(d). This feature in  $ab$ -axis magnetization may be associated with the distortion from hexagonal to orthorhombic structure expected for this material system [26,37,38]. In-plane lattice distortion in the  $ab$ -axis oriented sample is expected to produce spin canting away from the kagome plane which may result in reduced magnetization within the kagome plane. However, a

similar feature is absent for  $c$ -axis films. In our opinion, such structural distortions and resulting changes in magnetization may easily be masked by substrate-induced lattice strain in the epitaxial thin films at reduced thicknesses [39], and lattice strain up to 0.7–1.6% estimated for our films may have a significant effect on the structural and magnetic behavior of thin film  $Mn_3Ga$ .

For the  $c$ -axis case shown in Fig. 2(c), the zero-field cooled (ZFC) curve shows a decreasing magnetization with reducing temperature, whereas the field cooled (FC) curve shows an increasing magnetization which tends to saturate at low temperatures. On the other hand, for  $ab$ -axis orientation, both ZFC and FC curves show increasing magnetization with decreasing temperature, and these ZFC-FC observations along  $c$ -axis and  $ab$ -axis crystal orientation are consistent with previous reports on similar hexagonal  $Mn_3X$  systems [26,38,40]. The anisotropy in low field ZFC-FC behavior along  $ab$ -axis and  $c$ -axis may point to the anisotropic nature of magnetic interactions and the strain effects along these crystal directions [36,41,42].

### C. DC and terahertz anomalous Hall effect

The chiral antiferromagnets  $Mn_3Sn$  and  $Mn_3Ge$  are known to show anisotropic magnetotransport under magnetic fields along different crystal orientations [5,13,43,44]. Nonzero spontaneous AHE arises when the applied field is along the  $ab$ -axis (within the kagome plane formed by Mn moments with antichiral spin structure), while it vanishes for the field along the  $c$ -axis. Control over crystal orientation established in our films enables verification of such anisotropic transport signatures for our  $Mn_3Ga$  films. Figure 3(a) shows a comparison of AHE at 300 K for  $ab$ -axis and  $c$ -axis oriented samples. The  $ab$ -axis oriented film shows a nonzero spontaneous AHE while it disappears for  $c$ -axis orientation. This anisotropic behavior persists for the entire temperature range of the measurements 10–400 K. The temperature sweep measurements using the  $ab$ -axis oriented samples reveal that AHE shows a nonmonotonic behavior. In order to estimate the AHC ( $\sigma_{yx} = -\rho_{yx}/\rho_{xx}^2$ ) of the  $Mn_3Ga(40$  nm) layer, we estimate the anomalous Hall ( $\rho_{yx}^{Mn_3Ga}$ ) and longitudinal resistivity ( $\rho_{xx}^{Mn_3Ga}$ ) corresponding to the  $Mn_3Ga(40$  nm) layer, shown in Fig. 3(b), by accounting for the electrical current shunting through the  $W(7$  nm) buffer layer [19]. In Fig. 3(c) we combine the measurements performed in PPMS and a custom-built high-temperature probe to track the high-temperature evolution of the  $\rho_{yx}^{Mn_3Ga}(T)$  up to  $\approx 500$  K. Our data suggest  $\rho_{yx}^{Mn_3Ga}(T)$  approaches zero value at  $\approx 480$  K, confirming the expected  $T_N$  for our films, consistent with the  $T_N$  estimated from magnetization measurements shown in Fig. 2(b). Due to temperature limitations in our custom-built high-temperature probe we are unable to verify the AHE beyond 500 K. One expects the AHE to saturate close to zero value for temperature beyond  $T_N$ ; such behavior may also be witnessed in magnetization, which we verify in Fig. 2(b).

The temperature dependence of the zero-field  $\sigma_{yx}(T)$  estimated from the data in Fig. 3(b) is summarized in Fig. 3(d). As shown,  $-\sigma_{yx}(T)$  starts with  $19$  ( $\Omega \text{ cm}$ ) $^{-1}$  at 10 K, and goes through a maximum of  $28$  ( $\Omega \text{ cm}$ ) $^{-1}$  between 100 and 200 K and decreases to  $7$  ( $\Omega \text{ cm}$ ) $^{-1}$  with increasing temperature up

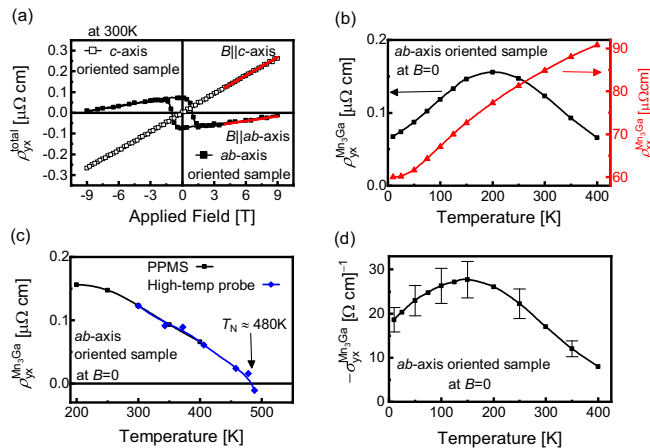


FIG. 3. DC anomalous Hall effect of *ab*-axis and *c*-axis oriented  $\text{Mn}_3\text{Ga}$ (40 nm) samples. (a) Field dependent total DC Hall resistivity  $[\rho_{yx}(B)]$  of *ab*-axis and *c*-axis oriented  $\text{Mn}_3\text{Ga}$ (40 nm) samples recorded at 300 K. Red solid lines show a linear fit to the high field (4.5–9 T) Hall data highlighting the slope. (b) Temperature dependent DC Hall resistivity  $[\rho_{yx}^{\text{Mn}_3\text{Ga}}(T)]$  and longitudinal resistivity  $[\rho_{xx}^{\text{Mn}_3\text{Ga}}(T)]$  corresponding to *ab*-axis oriented  $\text{Mn}_3\text{Ga}$  at zero magnetic field.  $\rho_{yx}^{\text{Mn}_3\text{Ga}}(T)$  and  $\rho_{xx}^{\text{Mn}_3\text{Ga}}(T)$  are estimated by accounting for the current shunting through the W(7 nm) buffer layer [19]. (c) High-temperature evolution of  $\rho_{yx}^{\text{Mn}_3\text{Ga}}(T)$ , suggesting  $\rho_{yx}^{\text{Mn}_3\text{Ga}} \approx 0$  at  $\approx 480$  K, which is close to the expected Néel temperature for  $\text{Mn}_3\text{Ga}$ . Square symbols refer to data measured in PPMS between 200 and 400 K, and diamond symbols refer to data measured in a custom-built high-temperature probe between 300 and 500 K. (d) Estimated DC anomalous Hall conductivity ( $\sigma_{yx} = -\rho_{yx}/\rho_{xx}^2$ ) from the data shown in panel (b), where error bars represent the possible variation in the estimated magnitude of  $\sigma_{yx}$ .

to 400 K. A systematic decrease in  $-\sigma_{yx}(T)$  for approaching 400 K is consistent with the behavior seen in  $\text{Mn}_3X$  ( $X = \text{Sn}, \text{Ge}$ ) [13,18,22,45] systems where AHE is suppressed upon approaching  $T_N$  of the materials.

The sign of AHE in our films is consistent with experimental reports on  $\text{Mn}_3X$  ( $X = \text{Sn}, \text{Ge}$ ) [13,18,19,22,45]. However, previous reports on  $\text{Mn}_3\text{Ga}$  have shown sign reversal for AHE including a transition to the behavior suggesting the topological Hall effect [26,27,38]. Such varying AHE signatures for  $\text{Mn}_3\text{Ga}$  indicate a sensitive role of the location of the Fermi level in the band structure [15]. In contrast to the previous works, our paper, particularly through AHE evolution up to 500 K, with an estimated  $T_N \approx 480$  K establishes that a large AHC up to  $28 (\Omega \text{cm})^{-1}$  indeed emerges from the topological band structure of the antiferromagnetic hexagonal  $\text{Mn}_3\text{Ga}$ . Further, a persistent value of AHC  $\approx 19 (\Omega \text{cm})^{-1}$  at 10 K might suggest that  $\text{Mn}_3\text{Ga}$  sustains Weyl points in the vicinity of its Fermi level and antichiral antiferromagnetic phase down to low temperatures [37,46], similar to  $\text{Mn}_3\text{Ge}$  and unlike  $\text{Mn}_3\text{Sn}$  which develops a spin-glass-like behavior [5,13]. Our high-quality  $\text{Mn}_3\text{Ga}$  films developed here, showing a large AHE and a large  $T_N$ , are ideal for clarifying the microscopic origin of electrical control of antiferromagnetic order in  $\text{Mn}_3X$  systems and their applications.

In Fig. 3(a), solid red lines highlight the field linear response of the  $\rho_{yx}(B)$  for  $B > 3$  T. The estimated high field slope ( $0.03 \mu\Omega \text{cm}/\text{T}$ ) for the *c*-axis orientation is about four

times larger compared to the slope ( $0.007 \mu\Omega \text{cm}/\text{T}$ ) for *ab*-axis orientation. Note that when the external field is applied along the *c*-axis, the Hall effect captures, along with the ordinary Hall effect, the AHE component from the scalar spin chirality emerging from the spin canting normal to the kagome plane formed by Mn moments. In such *c*-axis orientation, both ordinary and anomalous Hall components show linear field dependence; on the other hand, in the case of the *ab*-axis orientation, one can distinguish the dominant spontaneous AHE component from the field-linear term. Recent work on  $\text{Mn}_3\text{Sn}$  suggests that a large field-linear AHE in the *c*-axis orientation is a combined result of real and momentum space Berry phase [47].

To characterize terahertz AHE, we measure the complex transverse conductivity  $\sigma_{xy}(\omega)$  using a time-domain terahertz spectrometer (TDS) equipped with a 7 T superconducting magnet in a closed cycled helium cryostat. Figure 4(a) shows the schematic of our magneto TDS setup. We generate the terahertz pulses using a TOPTICA TeraFlash Pro. This system irradiates an InGaAs photoconductive antenna (PCA) with 1550-nm pulses through a fiber optic cable. The PCA is effectively a gapped dipole antenna with a semiconductor bridging the gap. By applying a voltage across the semiconductor and irradiating the gap with an optical pulse whose photon energy matches the band gap of the semiconductor, charge carriers are freed and accelerated by the external voltage and then recombine on picosecond timescales ( $1 \text{ ps} = 1/1 \text{ THz}$ ). The radiated terahertz pulse is thus polarized parallel to the dipole antenna of the PCA as  $E(t) \propto \frac{\partial j(t)}{\partial t}$ , where we will define the initial polarization of the beam to be along the  $\hat{x}$  direction. We then direct the terahertz beam using off-axis parabolic mirrors (OAPMs). We place the OAPMs in a so-called  $8f$  geometry, as shown in Fig. 4(a). This geometry ensures a relatively frequency-independent, tight focus at the sample position. The magnetic sample then rotates the beam via the Faraday effect such that it is elliptically polarized. After the sample a wire grid polarizer is placed such that it acts as a polarizing beam splitter, passing light polarized along  $\hat{y}$  and reflecting light polarized along  $\hat{x}$ . The two beams are then focused onto separate detectors. This allows us to simultaneously measure  $E_x(\omega)$  and  $E_y(\omega)$ . Noting that  $E_x \gg E_y$ , these quantities can be directly related to the complex Faraday rotation,  $\theta_f$ , by  $\theta_f(\omega) = \frac{E_y(\omega)}{E_x(\omega)}$ . To eliminate any systematic effects that may manifest as finite rotations we carry out an antisymmetrization, where  $\theta_f$  is averaged with opposite field values and then subtracted i.e.,  $\theta_{f,AS}(B) = \theta_f(B) - \frac{\theta_f(B) + \theta_f(-B)}{2}$ . In Figs. 4(b)–4(d) we focus on the terahertz optical AHE studied through  $\theta_f(\omega)$  measured at different temperature. We use  $\sigma_{xx}(\omega)$  and  $\theta_f(\omega)$  to obtain  $\sigma_{xy}(T)$  through the relation  $\sigma_{xy} = \theta_f(\sigma_{xx} + \frac{\partial}{\partial \omega})$ . Details of the terahertz conductivity  $\sigma_{xx}(\omega)$  are provided in Fig. S4 of the Supplemental Material [29].

Figure 4(b) shows the measured  $\theta_f(1.5 \text{ THz})$  at discrete field values as the sample is magnetized through a field hysteresis of  $\pm 2.5$  T at various temperatures. The *ab*-axis oriented  $\text{Mn}_3\text{Ga}$  film shows a significant  $\theta_f$  at  $B = 0$  while it vanishes for the *c*-axis oriented  $\text{Mn}_3\text{Ga}$  film, consistent with the DC AHE observed in Fig. 3(a) for these two crystal orientations. In the case of the *ab*-axis oriented  $\text{Mn}_3\text{Ga}$  film the measured  $\theta_f(T)$  displays a nonmonotonic behavior showing a maximum

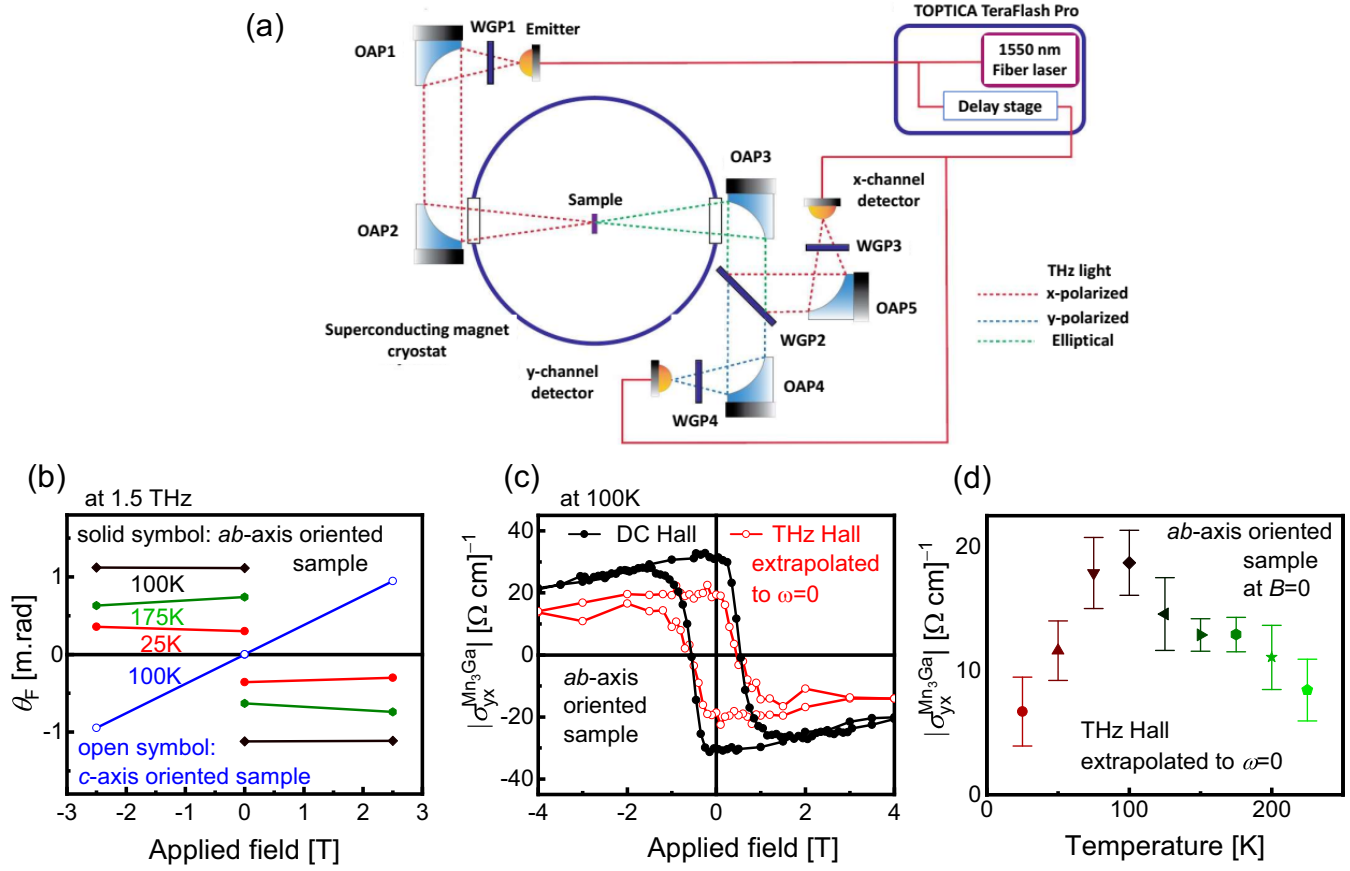


FIG. 4. Terahertz anomalous Hall effect of  $ab$ -axis and  $c$ -axis oriented  $\text{Mn}_3\text{Ga}$ (40 nm) samples. (a) Schematic of the magneto time-domain terahertz spectrometer used for measuring Faraday rotation. (b) Terahertz Faraday rotation for  $ab$ -axis and  $c$ -axis oriented  $\text{Mn}_3\text{Ga}$  samples recorded at various fixed temperatures and frequency of 1.5 THz, as the applied field is reduced to zero from  $\pm 2.5$  T. (c) Field evolution of terahertz Hall conductivity (estimated from field evolution of Faraday rotation) and its comparison with DC anomalous Hall conductivity for the  $ab$ -axis  $\text{Mn}_3\text{Ga}$  sample recorded at 100 K. For comparison, the terahertz Hall data are extrapolated to  $\omega = 0$  (see Fig. S3, Supplemental Material [29]). (d) Temperature evolution of terahertz Hall conductivity at zero field for the  $ab$ -axis oriented  $\text{Mn}_3\text{Ga}$  sample.

around 100 K. While this temperature evolution in the  $ab$ -axis oriented sample qualitatively reflects a trend similar to DC AHE, DC and terahertz Hall components seem to peak at different points within the broad and slowly varying AHC signal with temperature. These observations from the Hall transport correlate well with the subtle features captured in the temperature evolution of magnetization in the same temperature range for the  $ab$ -axis sample. Further, we would like to point out that possible lattice distortions in this temperature range might induce a topological Hall component coming from spin canting in real space. The combined result of real and momentum space Hall components and their temperature evolution may result in a local maximum in the measured Hall signal in DC and terahertz probes.

Finally, to further confirm the correlation of DC and terahertz AHE, in Fig. 4(c) we show the estimated magnitude of the terahertz AHC and its field evolution at 100 K. An entire hysteresis  $\sigma_{xy}^{\text{THz}}(\omega = 0)$  with  $B$  is estimated by measuring  $\theta_f(B)$ , tracking the field-induced switching of AHE between  $\pm 4$  T. Each data point in the  $\sigma_{xy}^{\text{THz}}(\omega = 0)$  vs  $B$  represents a linear extrapolation of  $\sigma_{xy}(\omega)$  to its zero frequency value (see Fig. S3, Supplemental Material [29]). As shown in Figs. 4(c) and 4(d), our result provides a qualitative agreement in the

field and temperature evolution of AHC and a comparable magnitude [48] between DC and terahertz probes.

#### D. Magnetoresistance

An important aspect of the Weyl semimetals is their anisotropic MR. Particularly, the chiral anomaly is known to be a signature for the breakdown of the number conservation law of the left- and right-handed Weyl fermions [13,49]. This leads to the NMR for  $B \parallel I$  configuration. In Fig. 5 we show the MR measurements on the  $ab$ -axis [Figs. 5(a)–5(c)] and  $c$ -axis [Figs. 5(d)–5(f)] oriented  $\text{Mn}_3\text{Ga}$  films. Our films do not show a clear characteristic sign reversal of MR from positive to negative sign, with changing  $B \perp I$  to  $B \parallel I$  configuration. However, the quantitative evolution of MR with field suggests that there is a clear enhancement in NMR for the  $B \parallel I$  case. This enhancement is quantified in Figs. 5(c) and 5(f) as  $\Delta\rho_{xx}(B \parallel I) - \Delta\rho_{xx}(B \perp I)$ , which confirms the enhanced NMR for the entire temperature range. While our observation is suggestive of chiral anomaly, we point out that MR in these thin films may be sensitive to the band structure, field, and temperature induced magnetic fluctuations, which are often present in the high field regime in these

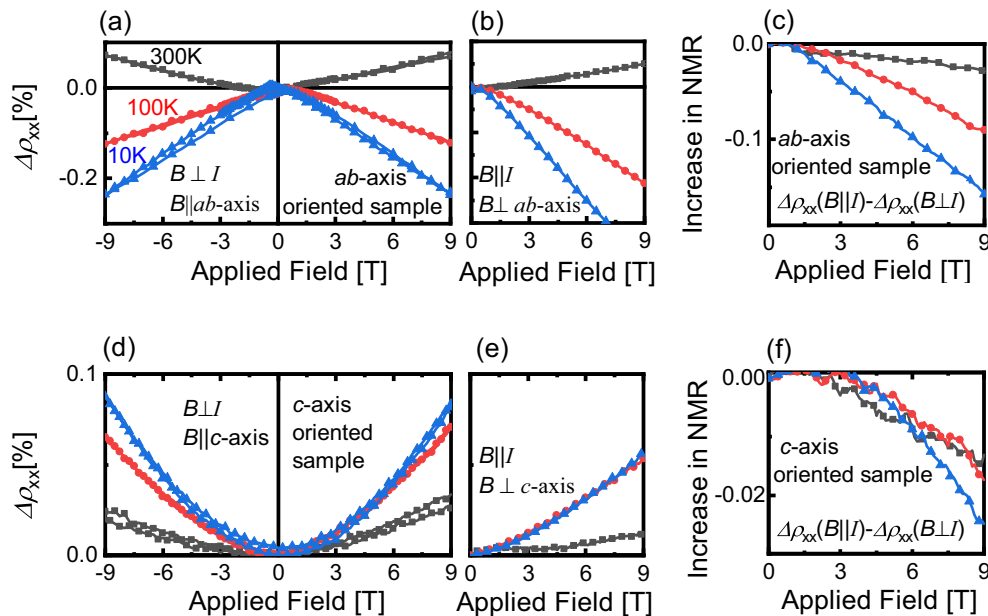


FIG. 5. Magnetoresistance for *ab*-axis and *c*-axis oriented  $\text{Mn}_3\text{Ga}$  films. (a, b) Magnetoresistance—( $\Delta\rho_{xx} = \frac{[\rho_{xx}(B) - \rho_{xx}(B=0)]}{\rho_{xx}(B=0)} \times 100$ ), measured for *ab*-axis oriented  $\text{Mn}_3\text{Ga}$  film at various temperatures in  $B \perp I$  and  $B \parallel I$  configuration respectively. (c) Increase in negative magnetoresistance (NMR), the difference of the data shown in panels (a) and (b) estimated as  $\Delta\rho_{xx}(B \parallel I) - \Delta\rho_{xx}(B \perp I)$  for *ab*-axis oriented  $\text{Mn}_3\text{Ga}$  film. (d, e) Magnetoresistance ( $\Delta\rho_{xx}$ ) measured for *c*-axis oriented  $\text{Mn}_3\text{Ga}$  film at various temperatures in  $B \perp I$  and  $B \parallel I$  configuration respectively. (f) Increase in negative magnetoresistance, the difference of the data shown in panels (d) and (e), estimated as  $\Delta\rho_{xx}(B \parallel I) - \Delta\rho_{xx}(B \perp I)$  for *c*-axis oriented  $\text{Mn}_3\text{Ga}$  film.

frustrated magnetic systems [49], leading to  $T$ -dependent spin scattering contributions. Such complex behavior of MR may mask the unambiguous identification of the chiral anomaly [1,44].

Our results presented in Figs. 5(a), 5(b), 5(d), and 5(e) reveal a distinct MR behavior for the *ab*-axis oriented sample compared with the *c*-axis case. In the *ab*-axis sample the MR is dominated by the field-linear term for both  $B \parallel I$  and  $B \perp I$  configurations, while in the *c*-axis sample MR is dominated by the field-quadratic term. Further, this linear and quadratic field dependence of MR seems to evolve with temperature. It is suggested that a linear MR with field in these  $\text{Mn}_3\text{X}$  systems may be suggestive of type-2 Weyl fermions compared to field-linear dependence in type-1 Weyl fermions [49,50]. Weyl fermions of type-2 are expected to emerge when there is a tilting of type-1 Weyl nodes, leading to distinct topological properties [51,52]. Further, the effect of lattice strain along different crystal orientations may result in anisotropic modifications of band structure and hence transport signatures [52]. A detailed calculation of electronic band structure, a systematic investigation of lattice strain effects, and angular dependence of MR are essential for understanding the anisotropic MR behavior in these strained  $\text{Mn}_3\text{Ga}$  samples.

### E. Exchange bias effect

The EB effect is a result of magnetic coupling at the interface between a ferromagnet (FM) and an antiferromagnet. A strong exchange coupling of the magnetic spins at the FM/AFM interface causes a delayed magnetization reversal of the FM layer, thereby shifting the FM hysteresis loop along the applied field axis. This interfacial effect is quantified by

EB field ( $B_{\text{EB}}$ ), a shift in magnetization with field,  $M(B)$  loop along the applied field direction. Often an increase in coercivity ( $B_C$ ) of the exchange biased FM layer is also seen as a consequence of EB. However,  $B_C$  of an FM layer might be influenced by the microstructure of the layer itself, independent of the interface. Here a shift in  $M(B)$  loop quantified by  $B_{\text{EB}}$  provides a conclusive signature of the interfacial origin of EB. Further, the direction of the  $B_{\text{EB}}$  in the FM/AFM bilayer can be controlled by the direction of the applied cooling field, providing additional confirmation for the interfacial nature of the phenomenon.

Figures 6(a) and 6(d) show the magnetization with field for  $\text{Mn}_3\text{Ga}(40 \text{ nm})/\text{NiFe}(10 \text{ nm})$  bilayers at 5 K under different FC protocols. A negative shift in the  $M(B)$  loop by 0.009 and 0.014 T is witnessed under a positive cooling field with *ab*-axis and *c*-axis oriented  $\text{Mn}_3\text{Ga}$ , respectively. Upon reversing the cooling field from +7 to -7 T, the shift in  $M(B)$  loop is shown to reverse its direction from the negative field axis to the positive.

To further probe the temperature evolution of  $B_C$  and  $B_{\text{EB}}$ , we measured the magnetoresistance of the  $\text{Mn}_3\text{Ga}/\text{NiFe}$  bilayers at various temperatures. Figures 6(b) and 6(e) show the normalized magnetoresistance data of  $\text{NiFe}(10 \text{ nm})$  at 10 and 100 K interfaced with the *ab*-axis and *c*-axis oriented  $\text{Mn}_3\text{Ga}$  layers, respectively. Typical signatures for the EB effect are seen, namely, MR vs  $B$  curves are shifted along the field axis, and the MR peak heights at  $B_{C1}$  and  $B_{C2}$  corresponding to the field sweeping down and sweeping up directions exhibit clear asymmetry [53–55]. One can estimate the layer  $B_C$  as the midpoint  $|(B_{C2} + B_{C1})/2|$  of the descending and ascending branches, and a shift in the hysteresis loop,  $B_{\text{EB}}$  as  $|(B_C - B_{C2})/2|$ .



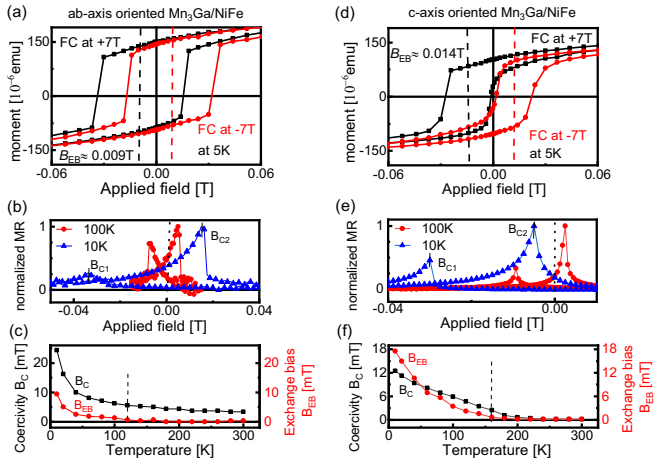


FIG. 6. Exchange bias effect in  $\text{Mn}_3\text{Ga}(40 \text{ nm})/\text{NiFe}(10 \text{ nm})$  bilayers. (a) Magnetization loop at 5 K for  $\pm 7 \text{ T}$  cooling field conditions for *ab*-axis oriented  $\text{Mn}_3\text{Ga}(40 \text{ nm})/\text{NiFe}(10 \text{ nm})$  bilayer. (b) Normalized magnetoresistance (MR) measured for *ab*-axis oriented  $\text{Mn}_3\text{Ga}(40 \text{ nm})/\text{NiFe}(10 \text{ nm})$  bilayer at 100 and 10 K. (c) Temperature evolution of exchange bias ( $B_{\text{EB}}$ ) and coercivity ( $B_{\text{C}}$ ) of the *ab*-axis oriented  $\text{Mn}_3\text{Ga}(40 \text{ nm})/\text{NiFe}(10 \text{ nm})$  bilayer estimated from MR measurements. (d) Magnetization loop at 5 K for  $\pm 7 \text{ T}$  cooling field conditions for *c*-axis oriented  $\text{Mn}_3\text{Ga}(40 \text{ nm})/\text{NiFe}(10 \text{ nm})$  bilayer. (e) Normalized MR measured for *c*-axis oriented  $\text{Mn}_3\text{Ga}(40 \text{ nm})/\text{NiFe}(10 \text{ nm})$  bilayer at 100 and 10 K. (f) Temperature evolution of  $B_{\text{EB}}$  and  $B_{\text{C}}$  of the *c*-axis oriented  $\text{Mn}_3\text{Ga}(40 \text{ nm})/\text{NiFe}(10 \text{ nm})$  bilayer estimated from MR measurements. Vertical dotted lines in panel (c) and (f) mark onset of exchange bias effect and the blocking temperature.

In Figures 6(c) and 6(f) we track the evolution of the  $B_{\text{C}}$  and  $B_{\text{EB}}$  with varying temperatures between 10 and 300 K for both the *ab*-axis and *c*-axis oriented  $\text{Mn}_3\text{Ga}/\text{NiFe}$  bilayers. It is evident that NiFe interfaced with the *c*-axis oriented  $\text{Mn}_3\text{Ga}$  shows relatively a larger  $B_{\text{EB}}$  of 0.018 T at 10 K, which decreases slowly with temperature. On the other hand, with the *ab*-axis oriented  $\text{Mn}_3\text{Ga}$  film, the maximum  $B_{\text{EB}}$  of 0.01 T is observed at 10 K and rapidly decreases with increasing temperature.  $B_{\text{EB}}$  remains finite at least up to 160 K for the *c*-axis oriented  $\text{Mn}_3\text{Ga}$  while it vanishes beyond 100 K for the *ab*-axis oriented  $\text{Mn}_3\text{Ga}$ . Another noticeable observation is the enhancement of  $B_{\text{C}}$  for NiFe interfaced *ab*-axis oriented  $\text{Mn}_3\text{Ga}$  film compared to the *c*-axis case, which indicates the microstructural differences in NiFe layer, affected by the underlying layers. A larger magnitude of  $B_{\text{EB}}$  and its temperature extent for *c*-axis orientation compared to the *ab*-axis case might indicate the distinct differences in magnetic coupling across the  $\text{Mn}_3\text{Ga}/\text{NiFe}$  interface with varying crystal orientation of the AFM  $\text{Mn}_3\text{Ga}$  layer and

the interfacial roughness. Notably, for NiFe grown *c*-axis oriented  $\text{Mn}_3\text{Ga}$  we expect the magnetization in NiFe to align parallel to the kagome spin structure formed in the underlying AFM. Such alignment of the easy axes of magnetization across the  $\text{Mn}_3\text{Ga}/\text{NiFe}$  interface may lead to a stronger magnetic coupling at the interface and hence a larger  $B_{\text{EB}}$ . For NiFe grown on *ab*-axis oriented  $\text{Mn}_3\text{Ga}$  film, we expect the easy axes of magnetization across the interface to be normal to each other leading to a decreased magnetic coupling and hence reduced  $B_{\text{EB}}$ . Our EB results confirm the interfacial magnetic interaction and the AFM nature of our  $\text{Mn}_3\text{Ga}$  films. Modeling these experimental observations through a detailed theoretical study may provide useful insights into the nature of magnetic domains, their stability, and the magnetic anisotropy in the three sublattice AFM  $\text{Mn}_3\text{X}$  systems.

### III. CONCLUSIONS

In summary, we have developed high-quality epitaxial  $\text{Mn}_3\text{Ga}$  films by a sputtering method. Different crystal orientations of hexagonal  $\text{Mn}_3\text{Ga}$  films grown on suitable substrates and buffer layers are confirmed by detailed XRD and HRTEM investigations. The temperature-dependent large AHC in the *ab*-axis oriented AFM  $\text{Mn}_3\text{Ga}$  indicates its topological origin, and the enhanced negative MR for  $B \parallel I$  configuration points to a chiral anomaly, a signature of a Weyl semimetallic state. Field linear and quadratic dependence of MR, its anisotropy with crystal orientation, and effects of lattice strain need further theoretical and experimental insights. Large  $T_{\text{N}} \approx 480 \text{ K}$  and the demonstration of EB effect further confirm the AFM nature of our films. Our observation of large optical AHE up to terahertz frequencies consistent with DC Hall transport highlights that our  $\text{Mn}_3\text{Ga}$  films are useful for developing future high-speed AFM spintronics.

### ACKNOWLEDGMENTS

The work at the Institute for Quantum Matter, an Energy Frontier Research Center, was funded by the U.S. Department of Energy, Office of Science, Basic Energy Sciences under Grant No. DE-SC0019331. This work was partially supported by the Japan Science and Technology Agency (JST) Mirai Program (Grant No. JPMJMI20A1), JST-CREST (Grant No. JPMJCR18T3), JST-AdCORP (JPMJKB2306), and New Energy and Industrial Technology Development Organization. The use of the facilities of the Materials Design and Characterization Laboratory at the Institute for Solid State Physics, The University of Tokyo, is gratefully acknowledged. This work was performed (in part) at the Materials Characterization and Processing Center in the Whiting School of Engineering at Johns Hopkins University.

- [1] N. Armitage, E. Mele, and A. Vishwanath, Weyl and Dirac semimetals in three-dimensional solids, *Rev. Mod. Phys.* **90**, 015001 (2018).  
 [2] V. Baltz, A. Manchon, M. Tsoi, T. Moriyama, T. Ono, and Y. Tserkovnyak, Antiferromagnetic spintronics, *Rev. Mod. Phys.* **90**, 015005 (2018).

- [3] S. Nakatsuji and R. Arita, Topological magnets: Functions based on Berry phase and multipoles, *Annu. Rev. Condens. Matter Phys.* **13**, 119 (2022).  
 [4] L. Šmejkal, A. H. MacDonald, J. Sinova, S. Nakatsuji, and T. Jungwirth, Anomalous Hall antiferromagnets, *Nat. Rev. Mater.* **7**, 482 (2022).



- [5] S. Nakatsuji, N. Kiyohara, and T. Higo, Large anomalous Hall effect in a non-collinear antiferromagnet at room temperature, *Nature (London)* **527**, 212 (2015).
- [6] T. Matsuda, N. Kanda, T. Higo, N. P. Armitage, S. Nakatsuji, and R. Matsunaga, Room-temperature terahertz anomalous Hall effect in Weyl antiferromagnet  $\text{Mn}_3\text{Sn}$  thin films, *Nat. Commun.* **11**, 909 (2020).
- [7] M. Kimata, H. Chen, K. Kondou, S. Sugimoto, P. K. Muduli, M. Ikhlas, Y. Omori, T. Tomita, A. H. MacDonald, S. Nakatsuji, and Y. Otani, Magnetic and magnetic inverse spin Hall effects in a non-collinear antiferromagnet, *Nature (London)* **565**, 627 (2019).
- [8] M. Ikhlas, T. Tomita, T. Koretsune, M.-T. Suzuki, D. Nishio-Hamane, R. Arita, Y. Otani, and S. Nakatsuji, Large anomalous Nernst effect at room temperature in a chiral antiferromagnet, *Nat. Phys.* **13**, 1085 (2017).
- [9] M. Mizuguchi and S. Nakatsuji, Energy-harvesting materials based on the anomalous Nernst effect, *Sci. Technol. Adv. Mater.* **20**, 262 (2019).
- [10] T. Higo, H. Man, D. B. Gopman, L. Wu, T. Koretsune, O. M. J. van't Erve, Y. P. Kabanov, D. Rees, Y. Li, M.-T. Suzuki, S. Patankar, M. Ikhlas, C. L. Chien, R. Arita, R. D. Shull, J. Orenstein, and S. Nakatsuji, Large magneto-optical Kerr effect and imaging of magnetic octupole domains in an antiferromagnetic metal, *Nat. Photon.* **12**, 73 (2018).
- [11] M. Wu, H. Isshiki, T. Chen, T. Higo, S. Nakatsuji, and Y. Otani, Magneto-optical Kerr effect in a non-collinear antiferromagnet  $\text{Mn}_3\text{Ge}$ , *Appl. Phys. Lett.* **116**, 132408 (2020).
- [12] H. C. Zhao, H. Xia, S. Hu, Y. Y. Lv, Z. R. Zhao, J. He, E. Liang, G. Ni, L. Y. Chen, X. P. Qiu, S. M. Zhou, and H. B. Zhao, Large ultrafast-modulated Voigt effect in noncollinear antiferromagnet  $\text{Mn}_3\text{Sn}$ , *Nat. Commun.* **12**, 5266 (2021).
- [13] T. Chen, T. Tomita, S. Minami, M. Fu, T. Koretsune, M. Kitatani, I. Muhammad, D. Nishio-Hamane, R. Ishii, F. Ishii, R. Arita, and S. Nakatsuji, Anomalous transport due to Weyl fermions in the chiral antiferromagnets  $\text{Mn}_3X$ ,  $X = \text{Sn, Ge}$ , *Nat. Commun.* **12**, 572 (2021).
- [14] T. Higo and S. Nakatsuji, Thin film properties of the non-collinear Weyl antiferromagnet  $\text{Mn}_3\text{Sn}$ , *J. Magn. Magn. Mater.* **564**, 170176 (2022).
- [15] Y. Zhang, Y. Sun, H. Yang, J. Zelezny, S. P. P. Parkin, C. Felser, and B. Yan, Strong anisotropic anomalous Hall effect and spin Hall effect in the chiral antiferromagnetic compounds  $\text{Mn}_3X$  ( $X = \text{Ge, Sn, Ga, Ir, Rh, and Pt}$ ), *Phys. Rev. B* **95**, 075128 (2017).
- [16] S. Tomiyoshi, S. Abe, Y. Yamaguchi, H. Yamauchi, and H. Yamamoto, Triangular spin structure and weak ferromagnetism of  $\text{Mn}_3\text{Sn}$  at low temperature, *J. Magn. Magn. Mater.* **54–57**, 1001 (1986).
- [17] Y. Chen, J. Gaudet, S. Dasgupta, G. G. Marcus, J. Lin, T. Chen, T. Tomita, M. Ikhlas, Y. Zhao, W. C. Chen, M. B. Stone, O. Tchernyshyov, S. Nakatsuji, and C. Broholm, Antichiral spin order, its soft modes, and their hybridization with phonons in the topological semimetal  $\text{Mn}_3\text{Ge}$ , *Phys. Rev. B* **102**, 054403 (2020).
- [18] Y. Takeuchi, Y. Yamane, J.-Y. Yoon, R. Itoh, B. Jinnai, S. Kanai, J. Ieda, S. Fukami, and H. Ohno, Chiral-spin rotation of non-collinear antiferromagnet by spin-orbit torque, *Nat. Mater.* **20**, 1364 (2021).
- [19] T. Higo, K. Kondou, T. Nomoto, M. Shiga, S. Sakamoto, X. Chen, D. Nishio-Hamane, R. Arita, Y. Otani, S. Miwa, and S. Nakatsuji, Perpendicular full switching of chiral antiferromagnetic order by current, *Nature (London)* **607**, 474 (2022).
- [20] D. Hong, N. Anand, C. Liu, H. Liu, I. Arslan, J. E. Pearson, A. Bhattacharya, and J. S. Jiang, Large anomalous Nernst and inverse spin-Hall effects in epitaxial thin films of kagome semimetal  $\text{Mn}_3\text{Ge}$ , *Phys. Rev. Mater.* **4**, 094201 (2020).
- [21] H. Tsai, T. Higo, K. Kondou, T. Nomoto, A. Sakai, A. Kobayashi, T. Nakano, K. Yakushiji, R. Arita, S. Miwa, Y. Otani, and S. Nakatsuji, Electrical manipulation of a topological antiferromagnetic state, *Nature (London)* **580**, 608 (2020).
- [22] H. Xie, X. Chen, Q. Zhang, Z. Mu, X. Zhang, B. Yan, and Y. Wu, Magnetization switching in polycrystalline  $\text{Mn}_3\text{Sn}$  thin film induced by self-generated spin-polarized current, *Nat. Commun.* **13**, 1 (2022).
- [23] X. Chen, T. Higo, K. Tanaka, T. Nomoto, H. Tsai, H. Idzuchi, M. Shiga, S. Sakamoto, R. Ando, H. Kosaki, T. Matsuo, D. Nishio-Hamane, R. Arita, S. Miwa, and S. Nakatsuji, Octupole-driven magnetoresistance in an antiferromagnetic tunnel junction, *Nature (London)* **613**, 490 (2023).
- [24] T. Matsuda, T. Higo, T. Koretsune, N. Kanda, Y. Hirai, H. Peng, T. Matsuo, N. Yoshikawa, R. Shimano, S. Nakatsuji, and R. Matsunaga, Ultrafast dynamics of intrinsic anomalous Hall effect in the topological antiferromagnet  $\text{Mn}_3\text{Sn}$ , *Phys. Rev. Lett.* **130**, 126302 (2023).
- [25] K.-R. Jeon, B. K. Hazra, K. Cho, A. Chakraborty, J.-C. Jeon, H. Han, H. L. Meyerheim, T. Kontos, and S. S. P. Parkin, Long-range supercurrents through a chiral non-collinear antiferromagnet in lateral Josephson junctions, *Nat. Mater.* **20**, 1358 (2021).
- [26] Z. H. Liu, Y. J. Zhang, G. D. Liu, B. Ding, E. K. Liu, Hasnain Mehdi Jafri, Z. P. Hou, W. H. Wang, X. Q. Ma, and G. H. Wu, Transition from anomalous Hall effect to topological Hall effect in hexagonal non-collinear magnet  $\text{Mn}_3\text{Ga}$ , *Sci. Rep.* **7**, 515 (2017).
- [27] F. Hu, G. Xu, Y. You, Z. Zhang, Z. Xu, Y. Gong, Er Liu, H. Zhang, E. Liu, W. Wang, and F. Xu, Tunable magnetic and transport properties of  $\text{Mn}_3\text{Ga}$  thin films on Ta/Ru seed layer, *J. Appl. Phys.* **123**, 103902 (2018).
- [28] B. Cheng, Y. Wang, D. Barbalas, T. Higo, S. Nakatsuji, and N. P. Armitage, Terahertz conductivity of the magnetic Weyl semimetal  $\text{Mn}_3\text{Sn}$  films, *Appl. Phys. Lett.* **115**, 012405 (2019).
- [29] See Supplemental Material at <http://link.aps.org/supplemental/10.1103/PhysRevMaterials.8.014204> for the experimental methods related to thin film growth, structural characterization of the thin films using x-ray diffraction, high-resolution transmission electron microscopy, magnetic characterization using a magnetic property measurement system, magnetotransport characterization using a physical property measurement system, optical characterization using terahertz optical and Faraday effects, additional data on rocking curve measurements, temperature-dependent DC transport, frequency-dependent Faraday effect, and terahertz optical conductivity. Supplemental Material also contains Refs. [19,28,34].
- [30] M. Boeije, L. van Eijck, N. van Dijk, and E. Brück, Structural and magnetic properties of hexagonal  $(\text{Mn,Fe})_{3-\delta}\text{Ga}$ , *J. Magn. Magn. Mater.* **433**, 297 (2017).

- [31] Y. You, H. Bai, X. Chen, Y. Zhou, X. Zhou, F. Pan, and C. Songa, Room temperature anomalous Hall effect in antiferromagnetic  $\text{Mn}_3\text{SnN}$  films, *Appl. Phys. Lett.* **117**, 222404 (2020).
- [32] D. Boldrin, A. P. Mihai, B. Zou, J. Zemen, R. Thompson, E. Ware, B. V. Neamtu, L. Ghivelder, B. Esser, D. W. McComb, P. Petrov, and L. F. Cohen, Giant piezomagnetism in  $\text{Mn}_3\text{NiN}$ , *ACS Appl. Mater. Interfaces* **10**, 18863 (2018).
- [33] J. Yoon, Y. Takeuchi, R. Itoh, S. Kanai, S. Fukami, and H. Ohno, Crystal orientation and anomalous Hall effect of sputter-deposited non-collinear antiferromagnetic  $\text{Mn}_3\text{Sn}$  thin films, *Appl. Phys. Express* **13**, 013001 (2020).
- [34] Y. Seto and M. Ohtsuka, ReciPro: free and open-source multi-purpose crystallographic software integrating a crystal model database and viewer, diffraction and microscopy simulators, and diffraction data analysis tools, *J. Appl. Cryst.* **55**, 397 (2022).
- [35] A. Markou, J. M. Taylor, A. Kalache, P. Werner, S. S. P. Parkin, and C. Felser, Noncollinear antiferromagnetic  $\text{Mn}_3\text{Sn}$  films, *Phys. Rev. Mater.* **2**, 051001(R) (2018).
- [36] M. Ikhlas, S. Dasgupta, F. Theuss, T. Higo, S. Kittaka, B. J. Ramshaw, O. Tchernyshyov, C. W. Hicks, and S. Nakatsuji, Piezomagnetic switching of the anomalous Hall effect in an antiferromagnet at room temperature, *Nat. Phys.* **18**, 1086 (2022).
- [37] H. Niida, T. Hori, and Y. Nakagawa, Magnetic properties and crystal distortion of hexagonal  $\text{Mn}_3\text{Ga}$ , *J. Phys. Soc. Jpn.* **52**, 1512 (1983).
- [38] L. Song, B. Ding, H. Li, S. Lv, Y. Yao, D. Zhao, J. He, and W. Wang, Observation of structural distortion and topological Hall effect in noncollinear antiferromagnetic Hexagonal  $\text{Mn}_3\text{Ga}$  magnets, *Appl. Phys. Lett.* **119**, 152405 (2021).
- [39] D. Kan and Y. Shimakawa, Strain effect on structural transition in  $\text{SrRuO}_3$  epitaxial thin films, *Cryst. Growth Des.* **11**, 5483 (2011).
- [40] A. K. Nayak, J. E. Fischer, Y. Sun, B. Yan, J. Karel, A. C. Komarek, C. Shekhar, N. Kumar, W. Schnelle, J. Kbler, C. Felser, and S. S. P. Parkin, Large anomalous Hall effect driven by a nonvanishing berry curvature in the noncolinear antiferromagnet  $\text{Mn}_3\text{Ge}$ , *Sci. Adv.* **2**, e1501870 (2016).
- [41] Q. Meng, P. Nie, L. Xu, J. Wang, S. Jiang, H. Zuo, X. Li, Z. Zhu, L. Balents, and K. Behnia, Magnetostriction, piezomagnetism and domain nucleation in  $\text{Mn}_3\text{Sn}$ , [arXiv:2301.06401](https://arxiv.org/abs/2301.06401).
- [42] A. Zelenskiy, T. Monchesky, M. Plumer, and B. Southern, Anisotropic magnetic interactions in hexagonal a b-stacked kagome lattice structures: Application to  $\text{Mn}_3\text{X}$  ( $\text{X} = \text{Ge}, \text{Sn}, \text{Ga}$ ) compounds, *Phys. Rev. B* **103**, 144401 (2021).
- [43] N. Kiyohara, T. Tomita, and S. Nakatsuji, Giant anomalous Hall effect in the chiral antiferromagnet  $\text{Mn}_3\text{Ge}$ , *Phys. Rev. Appl.* **5**, 064009 (2016).
- [44] D. Khadka, T. R. Thapaliya, S. H. Parra, X. Han, J. Wen, R. F. Need, P. Khanal, W. Wang, J. Zang, J. M. Kikkawa, L. Wu, and S. X. Huang, Kondo physics in antiferromagnetic Weyl semimetal  $\text{Mn}_{3+x}\text{Sn}_{1-x}$  films, *Sci. Adv.* **6**, eabc1977 (2020).
- [45] T. Higo, Y. Li, K. Kondou, D. Qu, M. Ikhlas, R. Uesugi, D. Nishio-Hamane, C. L. Chien, Y. Otani, and S. Nakatsuji, Omnidirectional control of large electrical output in a topological antiferromagnet, *Adv. Funct. Mater.* **31**, 2008971 (2021).
- [46] E. Krén and G. Kádár, Neutron diffraction study of  $\text{Mn}_3\text{Ga}$ , *Solid State Commun.* **8**, 1653 (1970).
- [47] X. Li, J. Koo, Z. Zhu, K. Behnia, and B. Yan, Field-linear anomalous hall effect and berry curvature induced by spin chirality in the kagome antiferromagnet  $\text{Mn}_3\text{Sn}$ , *Nat. Commun.* **14**, 1642 (2023).
- [48] R. Bhandia, B. Cheng, T. L. Brown-Heft, S. Chatterjee, C. J. Palmstrm, and N. P. Armitage, Thz-range faraday rotation in the Weyl semimetal candidate  $\text{Co}_2\text{TiGe}$ , *J. Appl. Phys.* **128**, 244303 (2020).
- [49] K. Kuroda, T. Tomita, M.-T. Suzuki, C. Bareille, A. A. Nugroho, P. Goswami, M. Ochi, M. Ikhlas, M. Nakayama, S. Akebi, R. Noguchi, R. Ishii, N. Inami, K. Ono, H. Kumigashira, A. Varykhalov, T. Muro, T. Koretsune, R. Arita, S. Shin, T. Kondo, and S. Nakatsuji, Evidence for magnetic Weyl fermions in a correlated metal, *Nat. Mater.* **16**, 1090 (2017).
- [50] V. A. Zyuzin, Magnetotransport of Weyl semimetals due to the chiral anomaly, *Phys. Rev. B* **95**, 245128 (2017).
- [51] M. Udagawa and E. J. Bergholtz, Field-selective anomaly and chiral mode reversal in type-II Weyl materials, *Phys. Rev. Lett.* **117**, 086401 (2016).
- [52] A. A. Soluyanov, D. Gresch, Z. Wang, Q. Wu, M. Troyer, X. Dai, and B. A. Bernevig, Type-II Weyl semimetals, *Nature (London)* **527**, 495 (2015).
- [53] A. Hoffmann, Symmetry driven irreversibilities at ferromagnetic-antiferromagnetic interfaces, *Phys. Rev. Lett.* **93**, 097203 (2004).
- [54] S. Brems, K. Temst, and C. Van Haesendonck, Origin of the training effect and asymmetry of the magnetization in polycrystalline exchange bias systems, *Phys. Rev. Lett.* **99**, 067201 (2007).
- [55] F. Radu, M. Etzkorn, R. Siebrecht, T. Schmitte, K. Westerholt, and H. Zabel, Interfacial domain formation during magnetization reversal in exchange-biased  $\text{CoO}/\text{Co}$  bilayers, *Phys. Rev. B* **67**, 134409 (2003).